CONFERENCE PRE-PRINT

TRANSPORT OF PRE-CHARACTERIZED TUNGSTEN DUST IN STOR-M

C. XIAO, N. NELSON, R. DAVIES, L. RYBALKA, L. COUËDEL University of Saskatchewan Saskatoon, Canada

Email: chijin.xiao@usask.ca

Abstract

Pre-characterised tungsten microparticles were injected into the STOR-M tokamak to study dust-plasma interactions under controlled conditions. The amount of in-vessel dust was regulated by varying the delay between dispenser activation and Ohmic discharge initiation. Dust trajectories, velocities, and accelerations were reconstructed from high-speed camera images, while ion Doppler spectroscopy provided plasma flow velocity measurements. Results show that dust experiences strong toroidal acceleration aligned with plasma flow which reverses when the plasma current and flow direction are reversed. A modified Barnes ion-drag model predicts forces within a factor of two of the experimental estimates, confirming ion drag as the dominant mechanism. Momentum analysis indicates that the plasma possesses sufficient momentum to account for the observed dust acceleration. Post-mortem sampling reveals size reduction and compositional changes downstream, suggesting selective transport, ablation, and possible contributions from native dust.

1. INTRODUCTION

Several pre-characterised dust injection experiments implementing three-dimensional tracking with fast video cameras have been conducted in different tokamaks, each employing its own dust injection system [1,2,3]. In NSTX, $40 \, \mu m$ lithium (Li) and $10 \, \mu m$ tungsten (W) dust were vertically injected into the Scrape-Off Layer (SOL) in separate campaigns. Both Li and W particles exhibited significant toroidal acceleration; however, W dust travelled more slowly in the toroidal direction while penetrating deeper into SOL than Li. When the toroidal magnetic field direction was reversed, W dust moved in the opposite vertical direction to Li [1]. In TEXTOR, carbon (C) dust smaller than $10 \, \mu m$ and W dust smaller than $5 \, \mu m$ were injected into SOL through a top port. Dust trajectories were reconstructed using the TRACE algorithm [2]. C dust exhibited complex motion due to irregular particle shapes and agglomerates, which occasionally fragmented within the plasma, whereas W dust trajectories appeared predominantly ballistic [3].

An extensive study of dust dynamics in the ASDEX Upgrade tokamak analysed four years of video data (2008 – 2012) imaging dust generated within the machine. Dust trajectories were reconstructed using TRACE. Similar to the pre-characterised dust injection experiments in TEXTOR, micrometre-sized particles exhibited motion largely governed by inertia, although their paths were generally aligned with the magnetic field lines [4].

In contrast to tracking native dust of unknown size and shape, injecting and tracking pre-characterised dust with known initial position, velocity, and size distribution offers clear advantages for studying dust transport in tokamaks. In this work, the plasma parameters examined differ significantly from those reported in earlier STOR-M studies [5]. To reduce the total amount of dust introduced and to avoid plasma disruptions caused by excessive dust, the dispenser bank voltage was lowered from 450 V to 400 V. For consistent operation, the micro-mesh screen was replaced with a slightly coarser weave, preventing sieve blockage and yielding an average injected particle diameter of $12.84\,\mu m$. This improvement was confirmed through bench tests of the dispenser [6] in which scanning electron microscopy (SEM) images of the injected dust further indicated that the dispenser design effectively prevented particle agglomeration.

This article is organised as follows. Section 2 describes the experimental setup for dust injection in STOR-M. Sections 3 and 4 present dust trajectories and the corresponding plasma parameters, respectively. In Section 5, a Barnes ion-drag model tailored to STOR-M plasma conditions is introduced and compared with experimental observations. Section 6 examines the momentum exchange between dust and ions, while Section 7 reports on post-mortem sampling of injected dust. Finally, Section 8 provides concluding remarks.

2. EXPERIMENT

Dust particles are introduced into the STOR-M tokamak $(R/a=46~{\rm cm}/12.5~{\rm cm},\,B_T=0.7~{\rm T},\,I_p=30~{\rm kA})$ from a top port prior to the STOR-M discharge, allowing a dust plume to fall and disperse within the chamber. The dispenser is mounted 35 cm above the tokamak mid-plane and its line of sight (LOS) is limited by a small port nipple, forming effectively an aperture of diameter 3.5 cm located 19.5 cm above the mid-plane. The cone-like column formed by the LOS of the dust dispenser has a diameter of approximately 8 cm on the mid-plane of STOR-M. Therefore, dust entering the chamber could be collimated by the geometry. Varying the delay time between activation of the dust dispenser and the Ohmic Heating (OH) discharge controls the fraction of the plume present in the plasma volume at the start of the STOR-M discharge.

Images of glowing dust in the plasma are captured using two synchronised high-speed cameras (Chronos 1.4). They are positioned at the same toroidal location. The side camera views horizontally from the low-field side, while the bottom camera views vertically from below. Both cameras record at 800×800 pixel resolution, with an exposure time of 1 μ s and a frame rate of 2156.3 frames/s. Both cameras provide a resolution of 121 ± 1 pixels/cm at their focal planes, corresponding to a field of view of 6.6 cm \times 6.6 cm. Minor differences in mounting result in focal depths of 4 cm for the side camera and 6 cm for the bottom camera. The depth of field over which objects remain discernible is approximately 12 cm for both cameras, covering the central region of the STOR-M plasma (with a cross-sectional diameter of 25 cm) along their respective line-of-view (LOV). The side camera captures the dust in STOR-M through a quartz window of 15 cm in diameter, but the view of the bottom camera is limited on the horizontal directions by its 5 cm diameter view port. Since the dust plume is elongated along the vertical direction, the bottom camera "sees" more dust particles in depth. However, the out-of-focus particles create a cloudy background, effectively reducing the number of trackable dust particles recorded by the bottom camera. Without the obscuring cloudy out-of-focus particles, the side camera tracks a larger number of dust particles compared to the bottom camera, making statistics more accurate.

3. DUST TRACKING RESULTS

Typical dust trajectories reconstructed for a delay time of $t_{\rm delay}=260$ ms between dust injection and STOR-M OH discharge are shown in Figure 1. Figure 1a displays snap-shots of reconstructed trajectories using images taken by the side camera at consecutive times after the start of the OH discharge. For this short delay time, most of the dust particles are above the mid-plane of the STOR-M tokamak and the plume diameter in this case appears to be approximately 6 cm. It is more important to note that the trajectories reveal a strong toroidal acceleration, causing the particles to deviate from their initial free-fall paths. Figure 1b shows dust trajectories determined from the bottom camera, taken at the same times as in Figure 1a. A pronounced toroidal velocity component is also observed, with negligible radial motion. Cloudy white areas appear in images of bottom camera frames due to glowing, out-of-focus particles, reducing the overall number of trackable particles. In addition, the plume diameter recorded appears to be only approximately 3 cm due to the small view port for the bottom camera, further reducing the number of dust particles recorded.

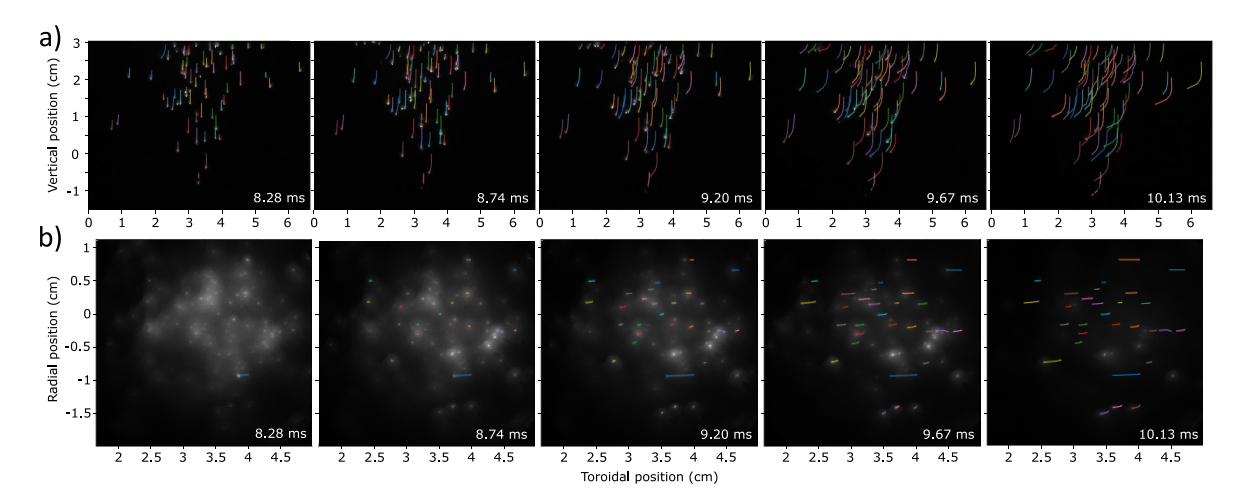


FIG. 1. Typical dust trajectories recorded simultaneously by (a) the side camera and (b) the bottom camera during a representative discharge with $t_{\rm delay}=260$ ms (shot number 363398). Times marked on each sub-frame indicate elapsed time since the start of the OH discharge.

Dust particle velocities are computed using a second-order Savitzky–Golay filter, a quadratic smoothing function applied to differentiate individual trajectories with respect to time. Velocities are evaluated at delay times of 270 ms, 320 ms, and 370 ms, based on 18, 13, and 5 discharges, respectively. Distributions of dust velocities across multiple discharges were all fitted to normal distributions. Figure 2a and Figure 2b show the initial and final velocity distributions, respectively, with fitted parameters μ (mean), σ (standard deviation), and n (sample size) indicated in the legends on the plots. With a long delay of 370 ms, the dust plume's centre of mass moves below the STOR-M mid-plane, and both cameras record systematically lower final speeds than the cases with shorter delays. For the side camera, abrupt trajectory termination as particles exit the field of view skew the final velocity distribution toward lower speeds. This effect arises from (i) radial expansion of the plume with delay time (shown in the dispenser characterisation [6]) and (ii) particles concentrated near the bottom of the frame due to the plume's centre-of-mass position. For the bottom camera, this skewed distribution of the final speed appear not only in the case with 370 ms delay but also with 320 ms, owing to the 5 cm diameter viewing port acting as a field stop, which truncates percentage-wise more trajectories than in the side view.

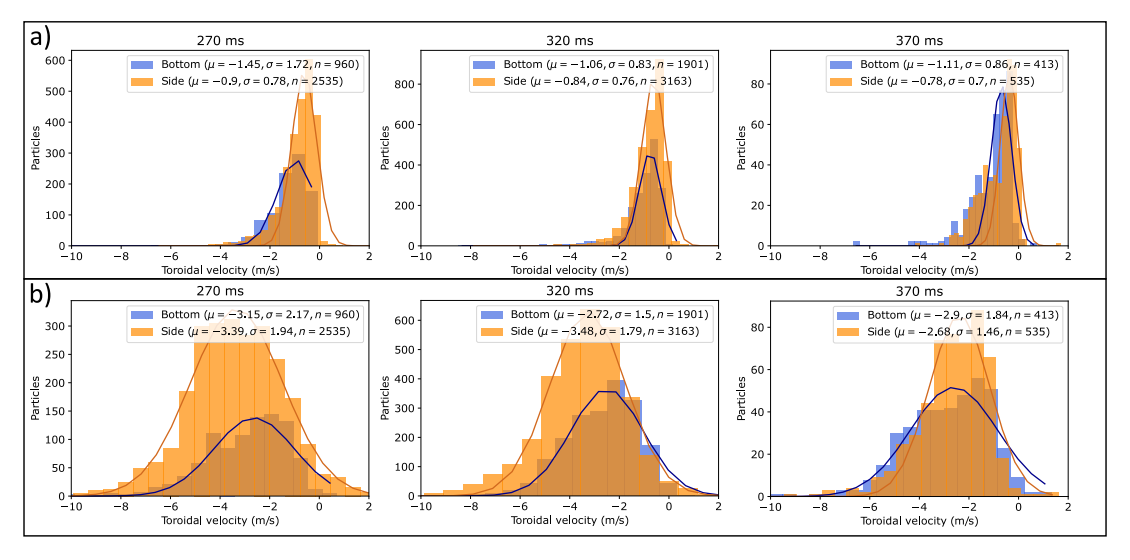


FIG. 2. Dust particle velocity distributions at delay times of 270 ms, 320 ms, and 370 ms for the side and bottom cameras. Statistics are based on 18, 13, and 5 discharges, respectively. (a) Initial velocity distributions; (b) final velocity distributions. The fitted parameters are shown in the legend (μ and σ in m/s).

Dust particle accelerations are obtained by applying a second-order Savitzky–Golay filter to the computed velocities. Figure 3 shows the distributions of mean acceleration fitted to normal curves at the same delay times as in Figure 2. The mean acceleration for each dust is average over its life time during which it is trackable. As with velocities, the acceleration distributions from the side and bottom cameras agree well at 270 ms and 370 ms. Fast-camera trajectories indicate that dust particles tend to experience increasing acceleration over time. Consequently, abrupt termination of trajectories (previously discussed) for the side camera at 370 ms and the bottom camera at 320 ms and 370 ms reduces the recorded mean acceleration and skews the distributions toward lower values.

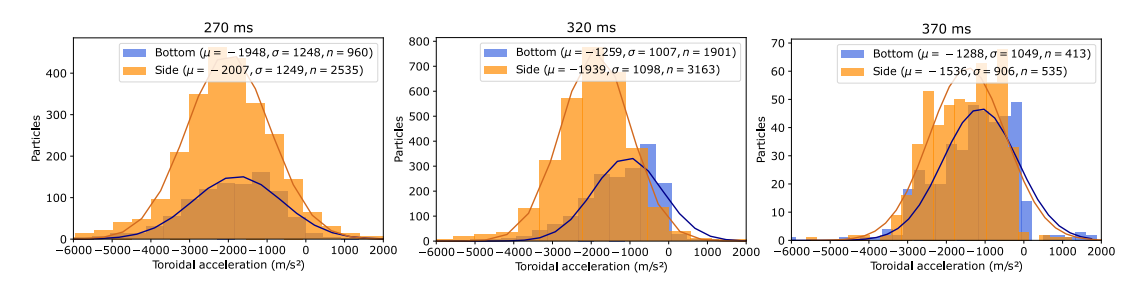


FIG. 3. Dust particle mean acceleration distributions derived from velocities in Figure 2. The fitted parameters are shown in the legend (μ and σ in m/s^2).

Finally, additional experiments were conducted in which the plasma current was reversed by changing the polarity of the OH coil connections to the capacitor bank. In these cases, the dust drift direction also reversed, consistent with the measured reversal of the plasma flow direction.

4. INFLUENCE OF DUST ON PLASMA FLOW VELOCITIES

Plasma parameters were recorded with and without tungsten dust injection over multiple discharges. Figure 4 shows these parameters as functions of time, with t=0 ms marking the start of OH discharge, for delays of $t_{\rm delay}=270$ ms (red), $t_{\rm delay}=250$ ms (green), and no dust injection (blue). Solid lines represent mean values over at least three shots, while shaded regions indicate standard deviations. Figures 4a–d display the loop voltage, plasma current, horizontal plasma position, and derived Spitzer electron temperature, respectively. A three-point moving average is applied to the electron temperature to smooth out fluctuations. The no-dust case represents the best plasma performance in terms of the plasma current amplitude. The amount of in-vessel dust increases with delay time within the chosen range and the plasma quality generally degrades as the dust amount increases, consistent with previous STOR-M dust injection studies [5], but less adversely since the total injected dust was intentionally reduced in this campaign. Additionally, the outward horizontal displacement of the plasma column during the plasma current ramp-up phase slows with increasing dust. Dust is visible between \sim 8-13 ms, during which loop voltage rises and the plasma current and temperature decreases, indicating reduced plasma performance.

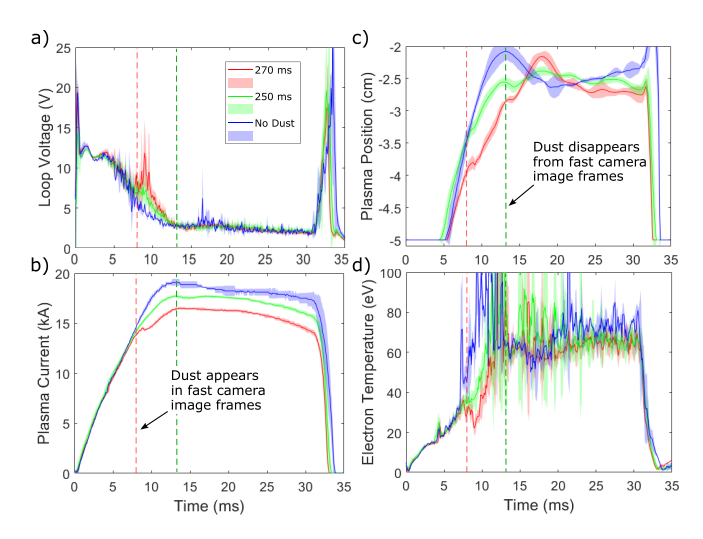


FIG. 4. Mean (solid lines) and standard deviation (shaded regions) of plasma parameters measured without dust injection and at delay times of 250 ms and 270 ms. Panels show: (a) loop voltage, (b) plasma current, (c) relative horizontal plasma displacement, and (d) electron Spitzer temperature. Dashed vertical lines mark the times at \sim 8 ms and \sim 13 ms after OH start when dust becomes visible and disappears, respectively.

Ion Doppler spectroscopy (IDS) was employed to measure the toroidal drift velocity of intrinsic carbon impurity ions with and without dust injection. Specifically, line emission from C-VI ions at 529.05 nm [7,8] was observed. Since C-VI is produced predominantly in the hot core of the STOR-M plasma, the measurement is limited to ions in this region. The hydrogen plasma flow velocity is assumed to be approximately equal to that of C-VI ions. Figure 5 shows the evolution of the measured velocities for various shots at different delay times, using the same colour scheme as in Figure 4. Positive flow velocity is defined in the plasma current direction (or opposite to the toroidal field direction). The measured plasma flow is largely negative, indicating a plasma flow in the counter-current direction (or in the toroidal field direction), which is consistent with the core plasma flow direction measured during previous STOR-M studies [9]. For the case without dust injection, flow becomes measurable about \sim 8 ms after the start of the OH discharge, \sim 1 ms earlier than in the cases with dust injection. This delay is likely due to dust-induced cooling, which slows plasma heating. Before $t \simeq 13$ ms, the flow speed is higher when less dust is present. After $t \simeq 13$ ms, when dust is no longer visible in camera frames, all measured flow velocities become more stable, regardless of the initial dust amount at the start of OH discharge. This indicates that ion flow tends to recover in STOR-M when dust is no longer present. The mechanism for this recovery remains under investigation and may be due to centrifugation of dust, re-deposition, and/or dust ablation, among other possible mechanisms.

5. BARNES MODEL OF ION-DRAG

The observed acceleration of dust particles in STOR-M is significant only in the toroidal direction, aligned with the measured plasma flow. Furthermore, experiments demonstrate that reversing the plasma current also reverses the dust drift direction, consistent with the measured reversal of the plasma flow. Whenever dust is visible in

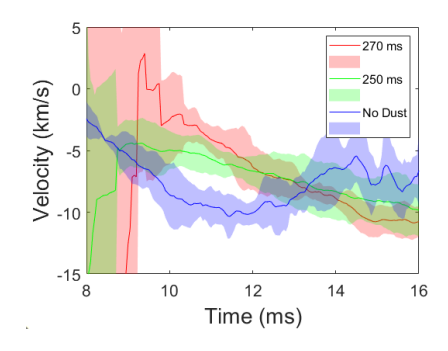


FIG. 5. Mean (solid lines) and standard deviation (shaded regions) of ion drift velocities measured without dust injection and with delay times of 250 ms and 270 ms. Positive toroidal velocity is defined in the plasma current direction.

camera frames, it exerts a measurable influence on plasma parameters and slows down the toroidal plasma flow speed. These findings suggest that the ion-drag force plays an important role in the dust dynamics observed in STOR-M.

To quantify the ion-drag force in STOR-M, a modified Barnes model [10,11] is employed. This model is based on binary Coulomb collisions between plasma ions and negatively charged dust particles. The resulting ion-drag force acting on a dust particle in a flowing plasma is expressed as:

$$\mathbf{F}_{id} = \frac{4\pi}{3} m_i n_i r_d^2 v_s \mathbf{u}_i \left(1 - \frac{2e\phi_d}{m_i v_s^2} \right) + \frac{8\pi}{3} \frac{n_i r_d^2 e^2 \phi_d^2}{m_i v_s^3} \mathbf{u}_i \ln \left(\frac{b_{90}^2 + (\lambda_D + r_d)^2}{b_{90}^2 + b_c^2} \right), \tag{1}$$

where m_i is the ion mass, n_i the ion density, r_d the dust radius, e the elementary charge, ϕ_d the dust potential, b_{90} the impact parameter for 90° ion deflection, b_c the maximum impact parameter for ion collection, λ_D the electron Debye length, $v_{th,i}$ the ion thermal velocity, \mathbf{u}_i the ion flow velocity, and $v_s = \sqrt{v_{th,i}^2 + u_i^2}$. Both b_{90} and b_c are functions of v_s

Solving Equation (1) requires a dust charging model. We treat the dust particle as a floating object that charges to the potential ϕ_d in order to balance collected currents from electrons and streaming ions. The electron current is given by [10]:

$$I_e(\phi_d) = -\pi r_d^2 n_e e \sqrt{\frac{8k_B T_e}{\pi m_e}} \exp\left(\frac{e\phi_d}{k_B T_e}\right),\tag{2}$$

while the streaming ion current is obtained based on a shifted Maxwellian distribution [10]:

$$I_i(\phi_d) = \pi r_d^2 n_i e v_{th,i} \sqrt{\frac{\pi}{4}} \gamma \left[\left(1 + \frac{1}{2\gamma^2} - \frac{e\phi_d}{k_B T_i \gamma^2} \right) \operatorname{erf}(\gamma) + \frac{1}{\sqrt{\pi} \gamma} \exp(-\gamma^2) \right], \tag{3}$$

where n_e is the electron density, k_B the Boltzmann constant, T_e the electron temperature, T_i the ion temperature, and $\gamma = u_i/v_{th,i}$.

The equilibrium potential is obtained by implicitly solving $I_e(\phi_d) + I_i(\phi_d) = 0$. The resulting solution is shown in Figure 6a, which presents the dust floating potential (ϕ_d) as a function of the ratio of ion drift velocity (u_i) to ion thermal velocity $(v_{th,i})$, for $T_e = 40 \text{ eV}$ and $T_i = T_e/3$. For a fixed flow velocity of $u_i = 8 \text{ km/s}$, the dependence of ϕ_d on ion temperature is shown in Figure 6b.

Figure 7a compares the theoretical ion-drag force, predicted by Equation (1) and normalised by $\pi a_d^2 n_i m_i v_{th,i}^2$, with the normalised experimental force. The latter corresponds to the force acting on an average 21 ng dust particle (pure W, average radius $\langle a_d \rangle = 6.4\,\mu\text{m}$) accelerating at $2~\text{km/s}^2$ (the approximate mean acceleration shown in Figure 3) through the plasma perturbed by the dust. Both theoretical and experimental forces are plotted as functions of $u_i/v_{th,i}$ for $T_e=40~\text{eV}$ and $T_i=T_e/3$, consistent with Figure 6a. Note that $v_{th,i}\approx 50$ –85 km/s. The theoretical ion-drag force and the experimental force derived from fast-camera trajectories agree reasonably well within experimental uncertainties.

The magnitude of the force acting on a dust particle with an average radius $\langle a_d \rangle = 6.4 \, \mu \text{m}$, assuming quasineutrality and a constant electron density of $5 \times 10^{18} \, \text{m}^{-3}$, is shown in Figure 7b as a function of ion temperature

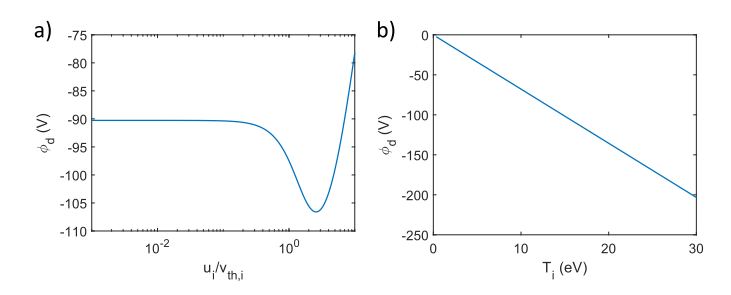


FIG. 6. (a) Dust floating potential as a function of the ratio of ion drift velocity to thermal velocity for $T_e = 40 \text{ eV}$ and $T_i = T_e/3$. (b) Dust floating potential as a function of ion temperature for $u_i = 8 \text{ km/s}$.

for various ion drift velocities. Taking the average acceleration of dust particles observed by the side camera ($\sim 2~{\rm km/s^2}$) and multiplying by the average particle mass (21 ng) yields an experimental force of approximately 42 nN. Comparing this value with the theoretical predictions in Figure 7b shows that a force of $\sim 20{\text -}65~{\rm nN}$ would act on dust particles in a plasma with an ion temperature of $10{\text -}20~{\rm eV}$ (reasonable for STOR-M) when the plasma flow velocity is between 4 and 8 km/s (as shown in Figure 5).

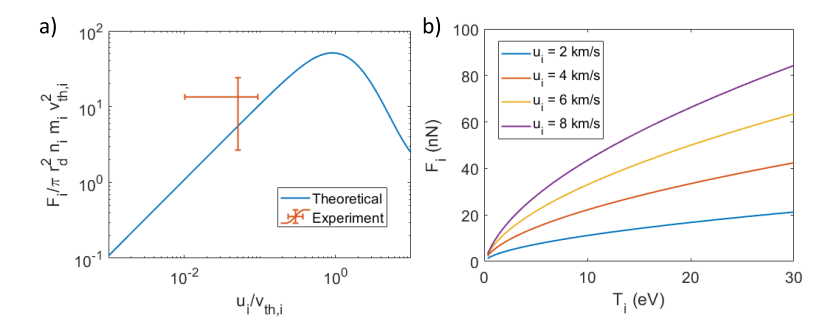


FIG. 7. (a) Theoretical ion-drag force predicted by Equation (1) and experimental force determined from dust trajectories (both normalised by $\pi a_d^2 n_i m_i v_{th,i}^2$), plotted as functions of the ratio of ion drift velocity to ion thermal velocity. (b) Ion-drag force in the STOR-M tokamak acting on particles of average radius 6.4 μ m, assuming constant ion density of 5×10^{18} m⁻³, plotted as a function of ion temperature for various flow velocities.

6. ION-DUST MOMENTUM TRANSFER

If the ion-drag force is indeed the primary mechanism responsible for the observed toroidal acceleration of tungsten dust, the plasma momentum $p_{\rm core}$ must be larger than the change in dust momentum $p_{\rm dust}$ within the STOR-M core:

$$p_{\text{core}} = n_i V_{\text{core}} m_p |u_i| > p_{\text{dust}} = N_d \langle m_d \rangle |\langle v_f \rangle - \langle v_i \rangle|, \qquad (4)$$

where $n_i = 5 \times 10^{18} \ \mathrm{m}^{-3}$ is the ion density, $V_{\mathrm{core}} = 0.016 \ \mathrm{m}^3$ is the volume of the STOR-M core region of radius (1/3)a where dust acceleration is observed (note, toroidal flow reversal was previously measured at a distance of (1/3)a from the plasma centre [9], consistent with our definition of the STOR-M's core region), m_p is the hydrogen ion mass, $u_i = 5 \ \mathrm{km/s}$ is the plasma flow velocity when dust motion is measurable, $N_d = 2000$ is the total number of injected dust particles (an upper bound for the number within the core), $\langle m_d \rangle = 21 \ \mathrm{ng}$ is the average dust particle mass, and $\langle v_f \rangle$ and $\langle v_i \rangle$ are the average final and initial toroidal velocities of dust particles, respectively. The average velocity change is $\sim 4 \ \mathrm{m/s}$, based on Figure 2. Evaluating Inequality 4 leads to:

$$p_{\text{core}} = 0.66 \text{ mg} \cdot \text{m/s} > p_{\text{dust}} = 0.17 \text{ mg} \cdot \text{m/s}, \tag{5}$$

demonstrating that the core plasma possesses roughly four times more momentum than the dust under conditions where significant toroidal motion is observed. This indicates that the plasma has sufficient momentum to transfer to dust particles injected into STOR-M.

7. POST-MORTEM SAMPLING

Dust sampling was performed in STOR-M following our initial experimental campaign reported in Ref. 5. Figure 8a shows a top view of the STOR-M tokamak and eight locations where carbon sticky tapes were pressed

onto the floor of the chamber to collect dust particles. Figure 8b presents the particle density on these tapes, determined from scanning electron microscope (SEM) images. Samples are grouped by toroidal locations. Samples 1–4, located near the dust dispenser, exhibit similar particle densities, whereas a noticeable decline is observed for samples 5 and 6, and again for 7 and 8, with increasing toroidal distance from the dispenser in the direction of dust motion. Using energy-dispersive X-ray spectroscopy (EDS) mappings, selected dust on the sample are associated with their dominant elemental composition and counted toward statistics. Figure 8c shows a bar chart of percentage number count based on the dominant elemental composition for: (i) the original pre-characterised dust (never exposed to the tokamak), (ii) sample 1 (near the dispenser), and (iii) samples 7 and 8 (far from the dispenser). As expected, the original dust consists almost entirely of tungsten. Dust from sample 1 is similar to the original dust, though some heavily oxidised material is present. On samples 7 and 8, tungsten remains dominant; however, there is a significant increase in compositional diversity compared to sample 1. This may result from (i) dust transported downstream within the plasma (with which dust interacts) and (ii) the presence of native dust produced by STOR-M components (e.g., probes and other plasma-facing elements) over decades of operation.

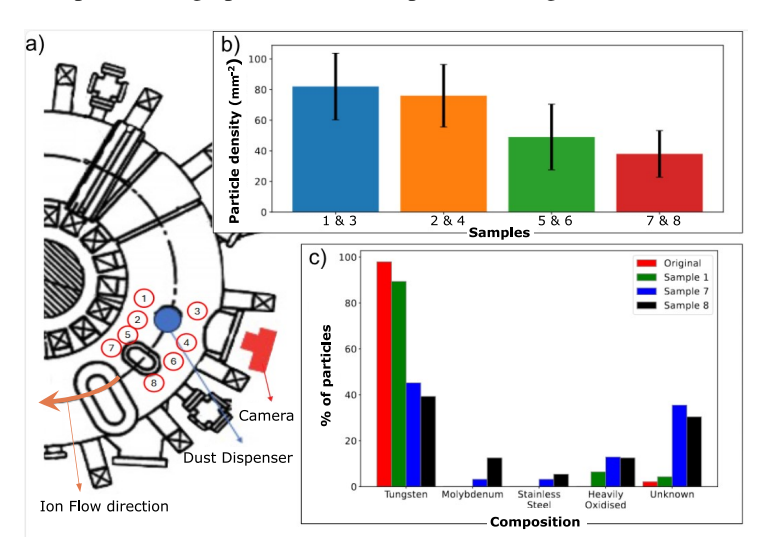


FIG. 8. Summary of dust samples collected from the floor of the STOR-M chamber using carbon sticky tapes. (a) Top view of STOR-M showing the eight sampling locations. (b) Particle number density on samples, counted from SEM images and grouped by toroidal position. (c) Relative chemical composition chart for particles of the original pre-characterised dust and for samples 1, 7, and 8, based on EDS.

To further investigate how dust deposits on the bottom of STOR-M, particle diameters in SEM images were manually measured for all samples to generate size distribution functions for the four toroidal locations where they were collected. Figure 9 shows histograms (blue) representing the probability distribution function (PDF) of particle diameters for: (a) samples 1 and 3, (b) samples 2 and 4, (c) samples 5 and 6, and (d) samples 7 and 8. These correspond to toroidal distances (clockwise from the dispenser) of approximately (a) -5 cm, (b) 5 cm, (c) 13 cm, and (d) 23 cm. All distributions fit well to a bimodal t-location-scale distribution (red curve, with fit parameters in the legend). This is expected, as the injected particles are t-location scale distributed about a mean corresponding to one of the components in the bimodal distribution at larger diameters (given by the green dashed curve). The second component (orange dashed curve) appears at smaller sizes and contributes increasingly more significantly to the overall distribution with increasing distance from the dust dispenser. Here, a and 1-aare normalisation coefficients ensuring that the two components sum to the red curve. These results suggest that dust transported downstream (i) may travel further if smaller in diameter, (ii) may undergo ablation, reducing its size while it moves along the toroidal direction by ion-drag, and/or (iii) may originate from other sources within STOR-M. It remains uncertain whether some of the additional dust was generated during tokamak operation or during maintenance and discharge cleaning; however, based on SEM images, it is indeed the case that the majority of additional dust was composed of injected micro-spheres.

8. CONCLUSION

In our experiments, tungsten dust with a known size distribution was injected from a calibrated dispenser into the STOR-M tokamak chamber prior to STOR-M discharges. The amount of in-vessel dust was controlled by varying the delay time, t_{delay} , between dispenser activation and Ohimc heating (OH) discharge initiation. By sweeping this delay, we quantified the impact of dust on plasma parameters for different initial plume positions and dust

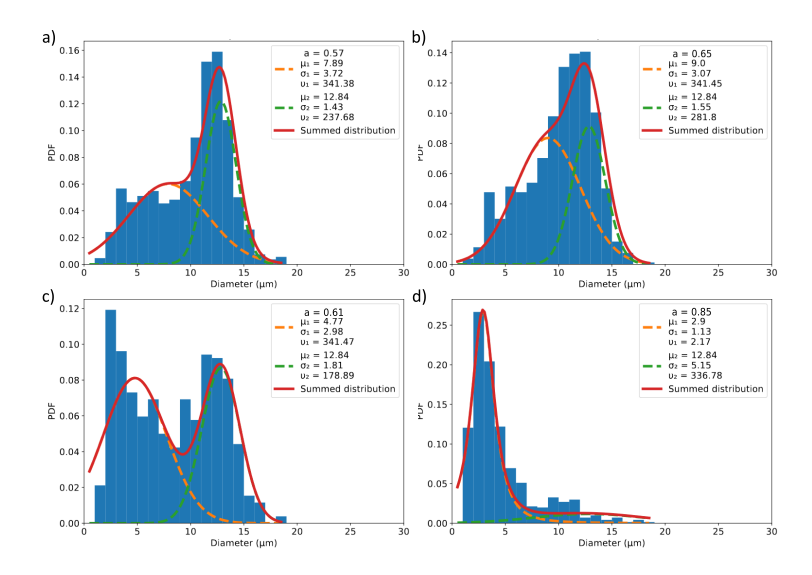


FIG. 9. Bimodal size distribution functions of dust collected from STOR-M at toroidal distances of (a) -5 cm, (b) 5 cm, (c) 13 cm, and (d) 23 cm relative to the dispenser downstream of the dust drift direction.

quantities at discharge onset. Simultaneously, the effect of plasma on dust motion was analysed using fast-camera imaging. In general, dust particles are accelerated in the plasma flow direction. The ion-drag force predicted from a non-magnetised Barnes model agrees within a factor of two with the values experimentally inferred from fast-camera trajectories. The observation of non-inertial tungsten dust trajectories is consistent with the behaviours reported in modern tokamaks, such as EAST, WEST, and ASDEX-Upgrade, employing tungsten plasma-facing components, in contrast to earlier pre-characterised tungsten dust experiments (e.g., TEXTOR). This discrepancy may arise because previous studies often reported clumping of injected dust, a phenomenon which is mitigated (confirmed by SEM imaging) in our work through dispenser characterisation. Post-mortem sampling of dust collected from the STOR-M chamber floor revealed a significant reduction in particle size and increased chemical compositional diversity downstream of the dust drift, or plasma flow, from the dispenser. The observed dust size distribution suggests selective transport of smaller particles, possible ablation during plasma exposure, and some contribution from native dust generated by long-term machine operation.

ACKNOWLEDGEMENTS

The research is supported by Natural Sciences and Engineering Research Council of Canada (NSERC) and the University of Saskatchewan.

REFERENCES

- [1] NICHOLS, J., ROQUEMORE, A.L., DAVIS, W., MANSFIELD, D.K., et al. 3-D reconstruction of pre-characterized lithium and tungsten dust particle trajectories in NSTX. J. Nucl. Mater. 415.1 (2011) S1098-S1101.
- [2] ENDSTRASSER, N., BROCHARD, F., ROHDE, V., BALDEN, M., et al. Video tracking and post-mortem analysis of dust particles from all tungsten ASDEX Upgrade. J. Nucl. Mater. 415.1 (2011) S1085-S1088.
- [3] SHALPEGIN, A., VIGNITCHOUK, L., EROFEEV, I., BROCHARD F., et al. Fast camera observations of injected and intrinsic dust in TEXTOR. Plasma Phys. Control. Fusion. 57.12 (2015) 125017.
- [4] BROCHARD, F., ROHDE, V., LUNT, T., LÓPEZ, G.S., et al. Intrinsic dust transport in ASDEX upgrade studied by fast imaging. Nucl. Mater. Energy. 18 (2019) 268-274.
- [5] NELSON, N., DAVIES, R., COUËDEL, L., and XIAO, C. Tungsten dust injection into the STOR-M tokamak. Radiat Eff Defect S. 178.11-12 (2023) 1344-1349.
- [6] NELSON, N., COUËDEL, L., and XIAO, C. Design and characterization of a dust dispenser for tungsten dust injection experiments in the STOR-M tokamak. Radiat Eff Defect S. 177.1-2 (2022) 181–197.
- [7] VAN ZEELAND, M.A., YU, J.H., BROOKS, N.H., HEIDBRINK, W.W., et al. Active and passive spectroscopic imaging in the DIII-D tokamak. Plasma Physics and Controlled Fusion 52.4 (2010) 045006.
- [8] SHUKLA, G., SHAH, K., CHOWDHURI, M.B., RAJ, H., et al. Observations of toroidal plasma rotation reversal in the ADITYA-U tokamak. Nuclear Fusion 59.10 (2019) 106049.
- [9] LIU, Y. Toroidal Flow Velocity Measurement in the STOR-M Tokamak by Ion Doppler Spectroscopy (2012).
- [10] MELZER, A., Physics of dusty plasmas, Vol. 962, Springer International Publishing, Cham, Switzerland (2019).
- [11] BARNES, M.S., KELLER, J.H., FORSTER, J.C., O'NEILL, J.A., et al. Transport of dust particles in glow-discharge plasmas. Phys. Rev. Lett. 68.3 (1992) 313.